

1. Introduction

About 60% of the energy produced worldwide is wasted in the form of heat. Therefore, the quest for high performance thermoelectric (TE) materials, which convert the waste heat to electrical energy in an environmental-friendly manner, has received enormous attention recently [1,2]. The Seebeck effect primarily governs the conversion of heat energy (waste heat or solar radiation) to electricity by a TE material [3]. A dimensionless parameter used to measure the performance of a TE material is the figure of merit (ZT), defined as $ZT = (\alpha^2 \sigma T) / K$, where α is the Seebeck coefficient, σ is the electrical conductivity, and K is the thermal conductivity ($K = K_e + K_l$) of the material and T is the temperature in Kelvin. To achieve a high ZT , both the Seebeck coefficient (α) and electrical conductivity (σ) of the material should be high, and its thermal conductivity (K) should be low [4,5]. However, due to the complex interplay between these parameters, obtaining a TE material with a high figure of merit is often tricky. Over the past few decades, considerable progress has been made in the thermoelectric field to enhance the power factor of the accessible TE materials such as Bi_2Te_3 , Sb_2Te_3 , PbTe [6–8], which operate at relatively low temperatures (<900 K). Bi_2Te_3 is an attractive TE material among the low bandgap semiconductors with the capability to convert solar energy [9–11] and waste heat [12,13] to electricity. Moreover, TE devices fabricated with Bi_2Te_3 material may convert heat energy even near room temperature (<400K) [14].

Several approaches were adapted to improve the ZT value of TE materials, primarily focusing on reducing the thermal conductivity (K_l) of their crystalline lattice, which is the major factor in reducing the ZT values of bulk semiconductors. One successful approach is the interstitial incorporation of smaller and heavier metal atoms such as actinide, lanthanide, alkaline-earth, alkali, and group IV elements, which act as active phonon scattering centres to reduce the K_l of the host lattice [15, 16]. On the other hand, low-dimensional thermoelectric materials manifest higher thermoelectric performance than their bulk counterparts due to the higher density of electronic states near the Fermi level, induced by quantum confinement and higher phonon scattering [17]. The Bi_2Te_3 nanostructures and thin films fabricated using chemical and physical methods [18–21] revealed enhanced thermoelectric performance compared to the performance of bulk Bi_2Te_3 . Mechanical alloying (MA) is a straightforward, fast, and cost-effective process among the physical methods utilized for fabricating TE nanostructures. It is one of the physical methods of nanomaterial synthesis [22]. The precursor powder materials are ball-milled for mechanical alloying (through fracture and re-welding mechanisms) under a controlled atmosphere to obtain the desired nanostructured material-specific crystal structure and microstructure [23]. It is also used for mixing powder ingredients, synthesizing nanocomposites and amorphous materials. Before ball milling, milling media (balls and vial) are selected according to the nature of precursor powders. For this purpose, different kinds of milling media such as Al_2O_3 , chrome steel, ZrO_2 , WC etc., balls of different diameters (1–20 mm) and vials of different volumes (50–500 mL) are available commercially [24]. Frequently, chrome steel milling media is used for metallic samples. Hard materials, such as ceramics are milled in other kinds of harder media. The ball mill instrument with available milling media needs to be optimized to obtain a desired nanocrystalline phase in a minimal milling duration. The optimized parameters are the number of balls, their diameter, the ball-to-powder mass ratio (BPMR), vial volume, speed (rpm) of the rotating disk, and the pause time between the milling and subsequent cooling steps [25]. These parameters can be optimized through several trial runs and kept fixed during the entire experiment. At first, the constituent precursor powders are mixed stoichiometrically according to the BPMR and loaded into the vial with an optimized number of balls of the same diameter. The vial containing balls and powder mixture is then sealed with its lid under a controlled atmosphere and placed on the rotating disk of the ball mill. The powder mixture within the vial is then milled with an optimized rpm of the

rotating disk of a high energy planetary ball mill. The milling is paused after an optimized duration, followed by subsequent cooling of milling media to room temperature before further milling. This milling process continues until the required nanocrystalline phase with desired microstructure is obtained. In general, it is a one-step “top-down” approach to prepare nanomaterials at room temperature with minimum numbers of ingredients in a short time. The main advantages of this synthesis process are: (i) one can have easy control over the structure and microstructure of the material, (ii) MA can synthesize almost any kind of nanomaterial within a short duration, (iii) nanometals, nanoalloys, nanoceramics, nanocomposites, and metal-ceramic-polymer nanocomposite blends can be easily synthesized, (iv) use of stoichiometric precursor powders reduces the possibility of formation of new phases, (v) materials with low and high melting temperatures can be easily milled together to form nanostructures or nanocomposites, (vi) no melting is needed to form an alloy or intermetallic compound, nanostructured phase can be obtained directly by this one-pot method, and so on. However, it has some limitations too: (i) there is every possibility that the milled powder gets contaminated from the milling media if the milling is done for a longer duration without any intermittent pause of milling, (ii) without proper optimization of all the milling parameters, we may not obtain the desired nanostructures, (iii) nanoparticles with desired morphology may not be obtained, (iv) obtained nanoparticles contain significant lattice strain, and (v) nanoparticles may agglomerate. MA was applied for size-controlled fabrication of n-type $\text{Bi}_2(\text{Se}, \text{Te})_3$ [26] and p-type $(\text{Bi}, \text{Sb})_2\text{Te}_3$ [27,28] nanoparticles. Nanostructures fabricated by this method had shown improved ZT values [29–33]. The ZT value of these TE nanostructures increases with the reduction of their particle size [34,35]. Hence the main purpose of this work is to synthesize thermoelectric Bi_2Te_3 nanostructures with an improved figure of merit in a more facile, time-effective and cost-effective manner and study the effect of thermal treatment on their microstructure and thermoelectric properties.

We have fabricated Bi_2Te_3 nanoparticles by mechanical alloying of elemental Bi and Te powders under the Ar atmosphere to study their thermoelectric properties. XRD and FESEM characterizations reveal the microstructure and the effect of thermal annealing on the structure, composition, and particle size of the synthesized nanostructures. The optical bandgap of the samples is measured utilizing Fourier-transformed infrared (FTIR) spectroscopy. Finally, the thermoelectric behaviours of the Bi_2Te_3 nanostructures and the effect of thermal annealing have been studied in 30–373K temperature range utilizing a physical property measurement system (PPMS). Here, a transition from semiconducting to metallic nature is observed owing to sintering the Bi_2Te_3 sample, which is reported for the first time and a moderately high value of ZT is obtained for cold-pressed mechanically alloyed Bi_2Te_3 sample, which is larger than the previously reported values of this sample under identical conditions (synthesized by MA and cold-pressed).

2. Experimental

2.1. Synthesis of Bi_2Te_3 nanoparticles

The Bi_2Te_3 nanoparticles were synthesized by ball milling of a stoichiometric (2:3 M ratio) mixture of analytical grade Bi and Te metal powders at room temperature, using a high-energy planetary ball mill (Model-P6, M/s FRITSCH, GmbH, Germany). The Bi (Loba Chemie; purity >99.5%) and Te (Sigma Aldrich, purity >99.5%) metal powder precursors were weighed accurately inside a glove box under Ar atmosphere and placed in a chrome steel vial (80 mL volume) filled with 30 chrome steel balls of 10 mm diameter, and sealed with its lid. The BPMR was optimized to 40:1. The sealed vial was then locked in the vial holder mounted on the rotating disk of the ball mill and rotated at 300 rpm. Several samples were prepared by milling the mixed precursors for different durations (15 min–10 h). The milling was paused after every

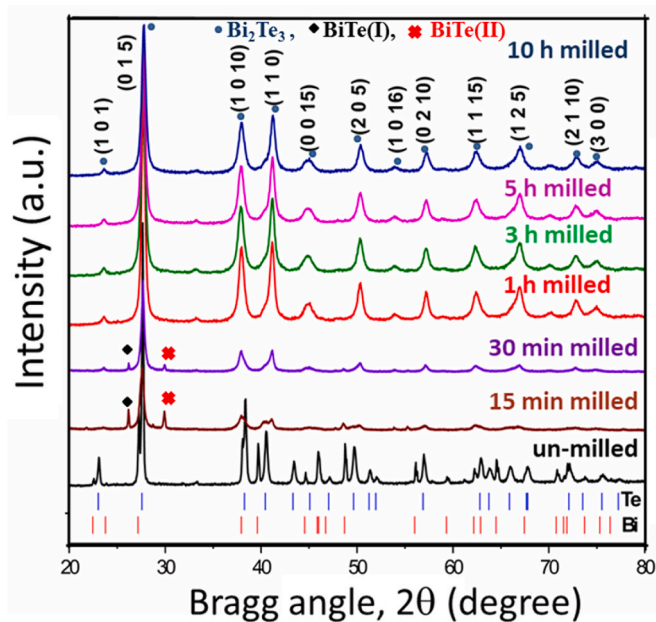


Fig. 1. X-ray powder diffraction patterns of un-milled and ball-milled Bi-Te powder mixture before annealing. Positions of the standard XRD peaks of metallic Bi and Te are shown as small solid bar markers at the bottom. Crystal planes of the Bi_2Te_3 phase are indexed in the XRD pattern of 10h ball-milled powder.

15 min to allow the hot vial to cool down (to room temperature) and avoid contamination from the milling media. Due to high energy impacts between the balls and the vial wall, a significant amount of heat is produced during milling, which can cause a surface softening effect of colliding balls and vial wall. As a result, loosely bound surface atoms of the balls and the vial can be detached from their surface during a prolonged milling process. However, introducing intermittent cooling steps in-between millings allows cooling the vial and the balls, reviving the strong bonding of their surface atoms, and avoiding sample contamination. After cooling the system to room temperature, milling was continued with the milled powder for longer durations. The total rotating time (excluding pauses) of the ball mill was considered in calculating the total milling time of the samples. After milling, the milled powder samples in the vial were collected inside the glove box (under Ar atmosphere) and stored in a vacuum desiccator. The 10 h ball-milled powder sample was pelletized using a stainless steel die-punch assembly (11 mm diameter) under 5.0 ton hydraulic pressure for 15 min. The thickness of the as-prepared pellets (before sintering) was about 1.5 mm. The pellet was annealed at 573K (at 2 °C/min heating rate) for 6 h inside a Carbolite tubular furnace under flowing Ar (200 ccm). Structural, microstructural, optical, and thermoelectric characterizations of the sintered and unsintered pellets were carried out to study the effect of thermal treatment.

2.2. Material characterization

X-ray diffraction (XRD) patterns of the un-milled, ball-milled, and the annealed (at 573K for 6 h under Ar flow) 10 h milled samples were recorded with Ni-filtered $\text{CuK}\alpha$ radiation ($\lambda = 1.5418 \text{ \AA}$) from an automated X-ray powder diffractometer (XRD, Bruker D8 Advance DaVinci) operated at 40 kV and 40 mA, in the 20°–80° 2θ range, with 0.02°/step and 30s/step counting time. Morphology, elemental compositions, and elemental mapping of each sample were revealed by analyzing FESEM images (Curl Zeiss, Sigma 300) and associated EDX (energy-dispersive X-ray) spectra. For estimating bandgap energy of the nanostructures, FTIR spectra of the annealed and unannealed samples were recorded in a Perkin-Elmer FRONTIER spectrometer in the 400–4000 cm^{-1} spectral

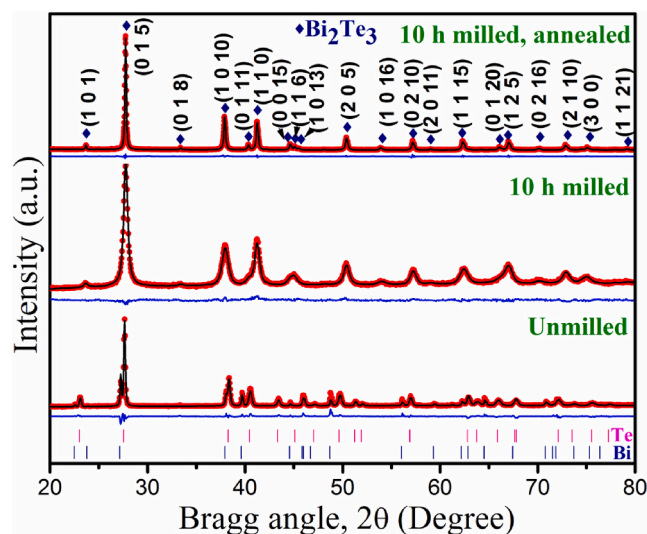


Fig. 2. The Rietveld analysis of the XRD patterns of un-milled, 10 h milled sample before and after thermal annealing. Solid red dots represent the experimental data points (I_0), continuous black lines represent the simulated patterns (I_c), and the continuous blue lines under respective diffraction patterns correspond to the difference between the experimental data (I_0) and simulated pattern (I_c). (For interpretation of the references to colour in this figure legend, the reader is referred to the Web version of this article.)

range. The powder samples were pelletized with dry KBr mixing in a 2:98 weight ratio for recording the FTIR spectra.

A Dynacool-9 physical properties measurement system (PPMS) of Quantum Design with thermal and electrical transport measurement options (TTO & ETO) was utilized to study the thermal and electrical properties of the pelletized samples in 30–370K temperature range. The sample temperature during these measurements was varied (increased or decreased) at 0.35 K/min. For thermoelectric measurements, both the as-prepared and heat-treated (annealed) pellet samples were first cut into rectangular pieces of about 8.5 mm × 4.9 mm sizes, polished over Buehler polishing sheet (using 10 μm alumina paste), washed with deionized (DI) water and dried in the air before mounting them in the TTO measuring paws of the PPMS. Then the samples were mounted on the TTO paws of PPMS using colloidal silver paint and Cu wires (0.2 mm diameter) to ensure suitable thermal and electrical contacts.

3. Results and discussion

3.1. Microstructure evaluation of Bi_2Te_3 nanoparticles

Fig. 1 represents the XRD patterns of the Bi_2Te_3 sample prepared at different milling times (15 min–10 h). For comparison, the XRD pattern of the un-milled sample (physical mixture of metal powders) is also presented in the figure, which contains only the reflections of elemental Bi (ICSD # 2446663) and Te (ICSD # 161690) metal powders. A significant change in the XRD pattern of the powder mixture is noticed only after 15 min of milling. While most of the reflections are broadened and overlapped, peak positions of the major reflections matched quite well with the Bi_2Te_3 (ICSD # 158366) phase, indicating the formation of the compound within a short duration of milling time. Two additional reflections appeared around the most intense (015) reflection of the Bi_2Te_3 phase correspond to BiTe(I) and BiTe(II) (ICSD # 9000678) phases [36]. Apart from these two reflections, no reflection corresponded to the precursor elements or any other phase.

After 30 min of milling, the content of secondary BiTe phases in the sample has reduced significantly, and the intensities of all Bi_2Te_3 reflections increase extensively. The XRD pattern of the 1 h milled sample contains only the reflections of the Bi_2Te_3 phase. With the increase of

Table 1

Structure and microstructure parameters of 10h milled un-annealed and annealed samples obtained from Rietveld refinement.

Structural parameters	10h milled un-annealed sample (average value)	10h milled annealed sample (average value)
Crystallite size (nm)	16.0	292.4
Lattice strain	3.0×10^{-3}	9.2×10^{-9}
Lattice parameters (Å)	a = 4.386 b c	4.387 30.426 30.426

milling time further (up to 10 h), intensities of all reflections increased gradually, without any trace of phase transition. However, with the increase of milling time, peak broadening increased gradually, indicating a reduction of crystallite size and subsequent increase in r.m.s. lattice strain in the Bi_2Te_3 nanostructures due to prolonged milling.

The Rietveld refinement outputs of the XRD patterns of the unmilled powder mixture and the 10 h ball milled Bi_2Te_3 powder before and after thermal annealing are shown in Fig. 2. The MAUD [37] software, based on simultaneous structure and microstructure refinements, was utilized for Rietveld refinement. Refinements reveal that all reflections in the XRD patterns of 10 h milled and annealed sample correspond to the Bi_2Te_3 phase (ICSD #158366).

While the XRD pattern of the un-milled sample is fitted jointly with Bi (ICSD # 2446663) and Te (ICSD # 161690) phases, XRD patterns of the un-annealed [36] and thermally annealed samples prepared by 10 h ball milling have been fitted with the Bi_2Te_3 (ICSD #158366) phase. In all three cases, the experimental XRD patterns fitted well with the simulated patterns with GoF (goodness of fit) values close to 1.0. As shown in Fig. 2, after thermal treatment, all the reflections of the Bi_2Te_3 phase became considerably sharp, indicating a significant grain growth

in the sample and a substantial reduction of r.m.s. lattice strain induced due to mechanical alloying. Some reflections appeared with weak intensities in the 10 h milled un-annealed sample due to peak broadening resulting from small crystallite size and high r.m.s. lattice strain, resolved clearly after thermal annealing (in Ar).

The crystallite sizes (D) and lattice strains (ϵ) of all as-prepared and thermally annealed 10 h milled samples were calculated from the ‘true’ peak broadening (β_t) considering all reflections according to the following eqns. [38,39] adopted in the Maud software [37]:

$$D = 0.9\lambda / \beta_t \cos\theta \quad (1)$$

$$\epsilon = \beta_t / 4\tan\theta \quad (2)$$

$$\beta_t = (\beta_{obs}^2 - \beta_{ins}^2)^{1/2} \quad (3)$$

where $\lambda = 1.5418 \text{ \AA}$ (Ni-filtered $\text{CuK}\alpha$ radiation), β_{obs} and β_{ins} are the full width at half maximum (FWHM) of diffraction peaks of experimental XRD patterns, and the instrumental broadening (FWHM) estimated from the Si standard (SRM 640, NIST), and θ is the Bragg angle in radians.

The structural and microstructural parameters obtained from Rietveld refinement of the XRD patterns of 10 h milled un-annealed and annealed samples are presented in Table 1. It can be noticed that after thermal annealing, the lattice parameters of the sample remain unchanged, while the average particle size increased substantially. Moreover, on thermal annealing, the anisotropic distribution of particle size [36] in the sample becomes isotropic (Fig. 3), indicating the right size homogeneity of the particles on prolonged thermal treatment.

Fig. 3 presents some typical FESEM images of the 10 h milled Bi_2Te_3 powder (Fig. 3(a)) and its thermally annealed compressed pellet (Fig. 3(c)), along with respective particle size distributions (Fig. 3(b) & (d)). As shown in Fig. 3(a), the as-prepared ball-milled particles are highly agglomerated, and the particle-matrix was porous before sintering.

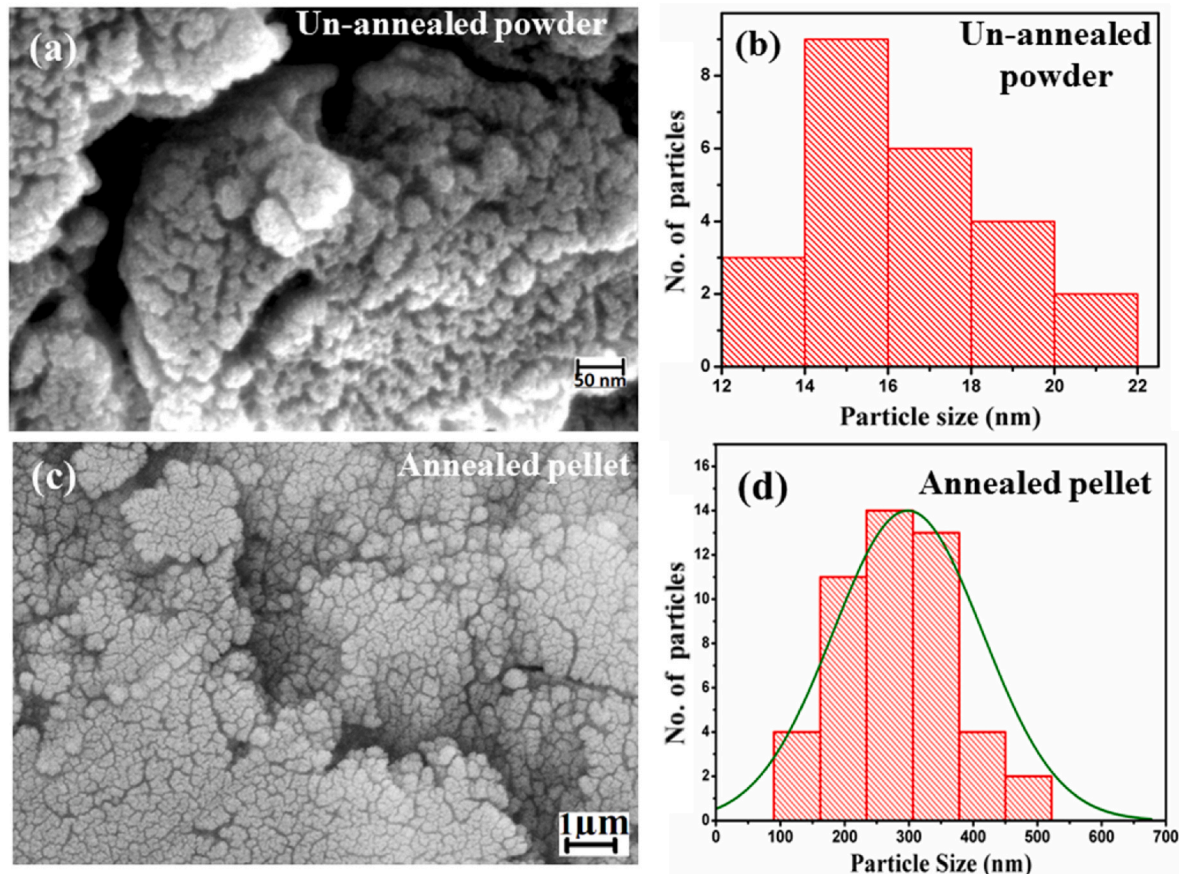


Fig. 3. Typical FESEM images (a,c) and particle size distribution histograms (b,d) of the 10 h milled Bi_2Te_3 sample, before and after its thermal annealing.

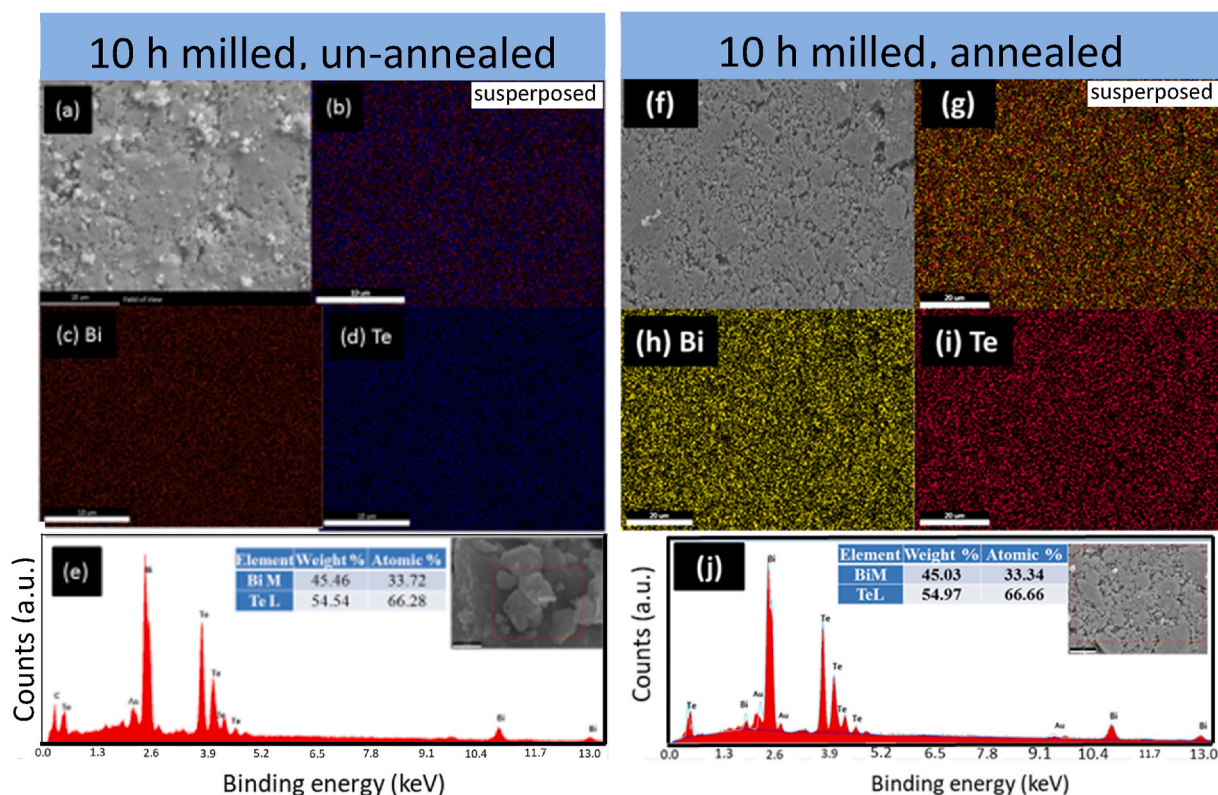


Fig. 4. (a) Secondary image, (b–d) elemental mapping images, and (e) typical EDX spectrum of the as-prepared 10h milled Bi_2Te_3 sample. (f) Secondary image, (g–i) elemental mapping images, and (j) typical EDX spectrum of the annealed 10h milled Bi_2Te_3 sample.

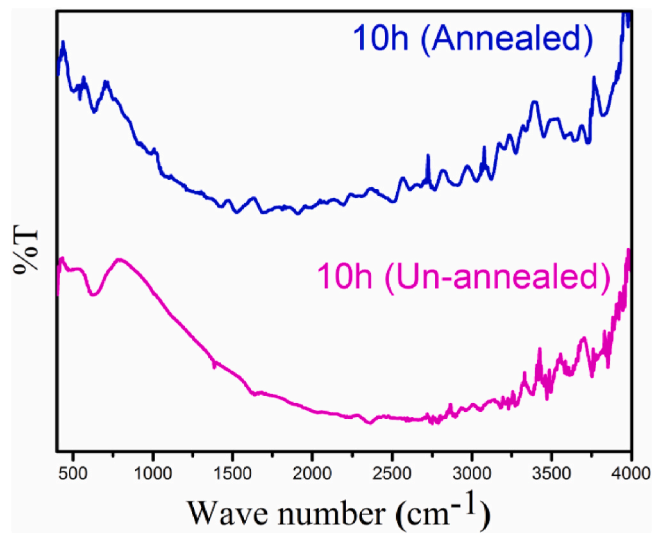


Fig. 5. FTIR spectra of 10 h milled Bi_2Te_3 sample before and after heat treatment.

However, the sample became compact on pelletization and thermal annealing (Fig. 3(c)). Particle sizes of the 10 h ball-milled powder and its sintered pellet are measured from FESEM images, and respective size distributions are presented in Fig. 3(b) and (d), respectively. The particle size of the unsintered sample varied between 12 to 22 nm, and that of the annealed sample varied between 80 to 520 nm, with an average of ~ 298 nm. It can be noticed that the particle sizes estimated from the FESEM images of the un-annealed and annealed samples agree well with the average crystallite size estimated from the Rietveld analysis of their XRD patterns (Table 1).

Fig. 4 presents elemental mapping images at the surface of annealed and un-annealed Bi_2Te_3 pellets prepared using 10h milled sample, along with their typical EDX spectra. EDX spectra of both the un-annealed and annealed samples revealed characteristic emissions of Bi and Te, along with the signals of Au and carbon (C). While the Au signal appeared from the Au film deposited over the pelletized samples to acquire their FESEM images, the carbon signal appeared from the carbon tape used to mount the samples over aluminium sample holders. As can be noticed, the Bi and Te elements are evenly distributed in both samples. The intensity of the carbon emission signal reduced substantially after annealing the sample. However, the EDX estimated Bi:Te atomic ratio in the un-annealed sample is close to 1:2, indicating a significant excess Te in the sample (inset of Fig. 4(e)). The Bi:Te atomic ratio in the sample remained almost unchanged after thermal treatment.

3.2. Bandgap determination of Bi_2Te_3 samples using FTIR spectra

Fig. 5 depicts the FTIR spectra of 10 h milled Bi_2Te_3 samples before and after thermal treatment. Transmittance values in the 400–4000 cm^{-1} spectral range are utilized to estimate their absorption coefficients (α) using the relation, $T = e^{-\alpha t}$, where T is the transmittance, and t is the thickness of the pelletized sample [40,41].

For estimating bandgap energy E_g of the samples of direct optical transition [40], we have utilized the Tauc relation:

$$\alpha h\nu = A(h\nu - E_g)^{1/2} \quad (4)$$

where h is Planck's constant, ν is the frequency of incident light, and A is a constant. The optical band gap energies of the samples are estimated by extrapolating the linear portion of $(\alpha h\nu)^2$ vs $h\nu$ plots to intercept the abscissa at zero ordinate (Fig. 6).

Fig. 6 shows the Tauc plots of the 10 h milled un-annealed and annealed Bi_2Te_3 samples. Tauc plots of both the samples revealed clear linear sections near their absorption edges. The bandgap energies

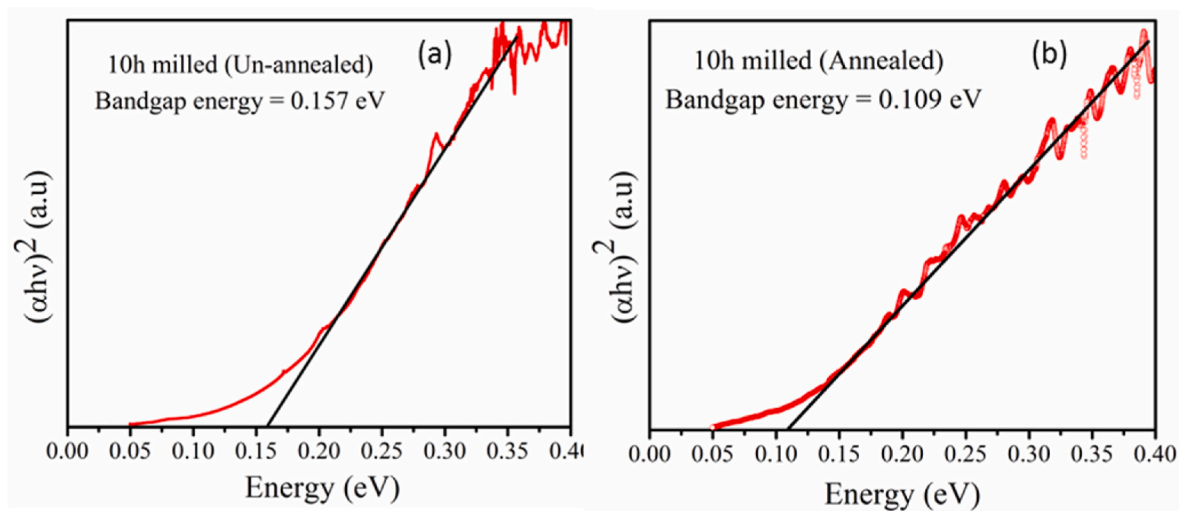


Fig. 6. $(\alpha h\nu)^2$ vs $h\nu$ plots (Tauc plots) for (a) 10 h milled un-annealed and (b) 10 h milled annealed Bi_2Te_3 samples.

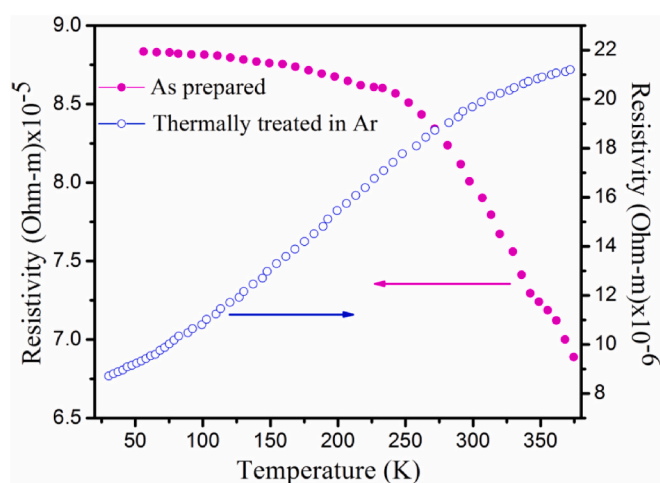


Fig. 7. Temperature variation of electrical resistivity of the 10 h milled Bi_2Te_3 sample before and after thermal treatment.

estimated by extrapolating the linear portion of the plots are 0.157 eV and 0.109 eV for un-annealed and annealed samples, respectively. The bandgap energy value of the un-annealed sample matches quite well with the previously reported band gap energy value of Bi_2Te_3 (0.15 eV) [40,42]. At the same time, the optical band gap energy (~ 0.109 eV) of the thermally treated sample matches well with the value (~ 0.11 eV) reported by Mishra et al. [43].

From Fig. 6, it can be seen that the bandgap energy of the 10 h milled sample has reduced after annealing, which in general, is associated with the comparatively larger crystallites of the annealed sample, as obtained in the XRD (Fig. 2) pattern and FESEM (Fig. 3) image analyses. It appears that due to sintering-assisted grain growth (>ten times), most of the lattice imperfections generated through mechanical alloying have been eliminated, and the separation between valance band (VB) and conduction band (CB) reduces significantly [44]. Hence one may say the sample is turning towards metallic nature with annealing done.

3.3. Electrical and thermoelectrical behaviour of the Bi_2Te_3 nanostructures

3.3.1. Electrical resistivity

Fig. 7 depicts the temperature variation of electrical resistivity for

the pelletized 10 h milled Bi_2Te_3 sample before and after thermal annealing (at 573 K, 6 h, in Ar atmosphere). As it is evident in the figure, for the entire temperature range (30–375 K), the electrical resistivity of the as-prepared (un-annealed) sample is about one order higher than that of the annealed sample indicating the occurrence of thermally-induced grain growth in the latter sample. The resistivity of the as-prepared sample decreased slowly with the increase of temperature up to ~ 250 K, and then rapidly until 375 K. Such a temperature-dependent behaviour of resistivity of the un-annealed sample demonstrates the semiconducting nature of the sample before annealing. However, after thermal annealing resistivity of the sample, apart from one order of reduction in magnitude (compared to that of the un-annealed sample), it increases with the increase of temperature, revealing its metallic nature. So it can be said that temperature-induced semiconductor to metal transition [45] has occurred here. However, this transition is not a pure semiconductor–metal transition because of the finite bandgap (0.109 eV) of the annealed sample. Instead, the thermal annealing turned the 10 h milled sample to a highly degenerate semiconductor of metallic character. Such a typical resistive behaviour of degenerate semiconductors was also reported in previous studies [46,47]. The structural and optical characterizations (Figs. 2, 3 and 6(b)) of the thermally annealed sample have revealed an extensive grain growth (more than 10 times) of the 10 h milled sample, along with a reduction in bandgap energy. It primarily reveals the nondegenerate to highly degenerate semiconducting transitions. It can be noticed in Fig. 7 that, for a particular temperature, the electrical resistivity of the sample decreased by about an order of magnitude after thermal treatment. The lower porosity of the sintered sample might also contribute to it, as porosity plays a vital role in the thermoelectric, electrical and thermal transport properties [48]. Due to substantial grain growth and porosity reduction, majority carrier mobility in the thermally annealed sample is expected to be very high, which has been reflected in its electrical resistivity. The room temperature electrical resistivity (ρ) of the 10 h milled sample has reduced from $7.974 \times 10^{-5} \Omega\text{-m}$ to $1.946 \times 10^{-5} \Omega\text{-m}$ after thermal annealing, which agrees well with the reported results of Takashiri et al. [49] for nanocrystalline Bi_2Te_3 thin films.

3.3.2. Thermal conductance and thermal conductivity

Fig. 8(a) presents the temperature variation of thermal conductance for the 10 h milled Bi_2Te_3 sample before and after its thermal annealing. Thermal conductivity (K) is estimated from thermal conductance (C) using the relation $K = C (l/A)$, where l is the distance between two thermometer shoes, and A is the cross-sectional area of the rectangular sample. As can be noticed, the thermal conductance of the un-annealed

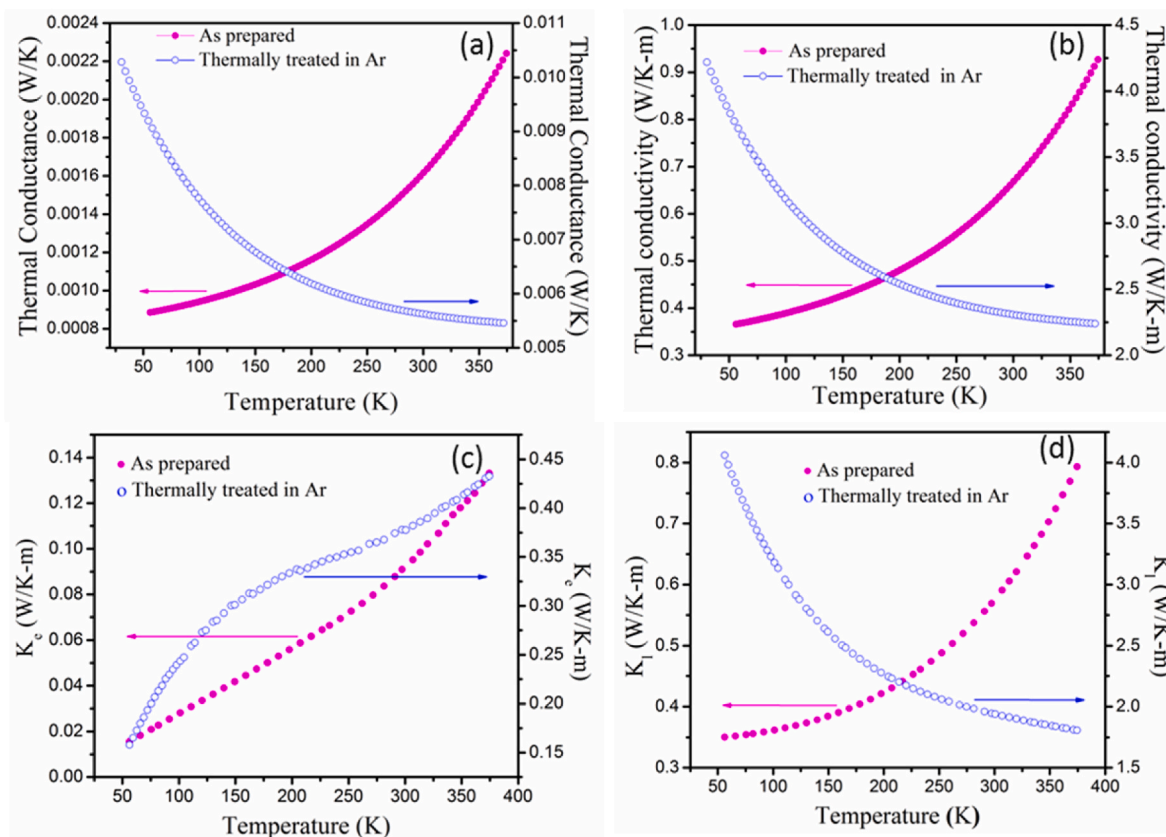


Fig. 8. Temperature variation of (a) thermal conductance, (b) total thermal conductivity, (c) electronic thermal conductivity, and (d) lattice thermal conductivity of the un-annealed and annealed Bi₂Te₃ samples prepared by 10h ball milling.

sample increases with temperature, while it decreases with temperature in the annealed sample. As expected, the temperature dependence of thermal conductivity of the samples (Fig. 8(b)) also revealed the same trend. Thus, the thermal conduction behaviour of the un-annealed and annealed samples has revealed their semiconducting and metallic (highly degenerate semiconductor) behaviour, respectively, which entirely agrees with their electrical and optical behaviours.

Generally, the total thermal conductivity (K) of a crystalline material is composed of lattice thermal conductivity (K_l) and electronic thermal conductivity (K_e) as, $K = K_l + K_e$. Electronic thermal conductivity can be determined from the electrical conductivity (as calculated from the measured value of electrical resistivity) using the Wiedemann-Franz law, $K_e = \sigma LT$, with Lorentz number, $L = 2.45 \times 10^{-8} \text{ W}\Omega/\text{K}^2$. Fig. 8(c)

shows the variation of electronic thermal conductivity with temperature. For both the un-annealed and annealed samples, K_e increases almost linearly with temperature. However, it increased faster in the annealed sample due to its higher electrical conductivity. On the other hand, the temperature dependence of lattice thermal conductivity K_l (Fig. 8(d)) of the samples revealed a similar trend as their total thermal conductivity.

Due to the semiconducting nature of the un-annealed sample, an increase in temperature generates a higher number of charge carriers in it. These charge carriers with high kinetic energy contributed to the thermal conduction and have enhanced the thermal conductivity of the materials at higher temperatures. However, upon thermal annealing, the semiconducting Bi₂Te₃ transforms into a degenerate semiconductor

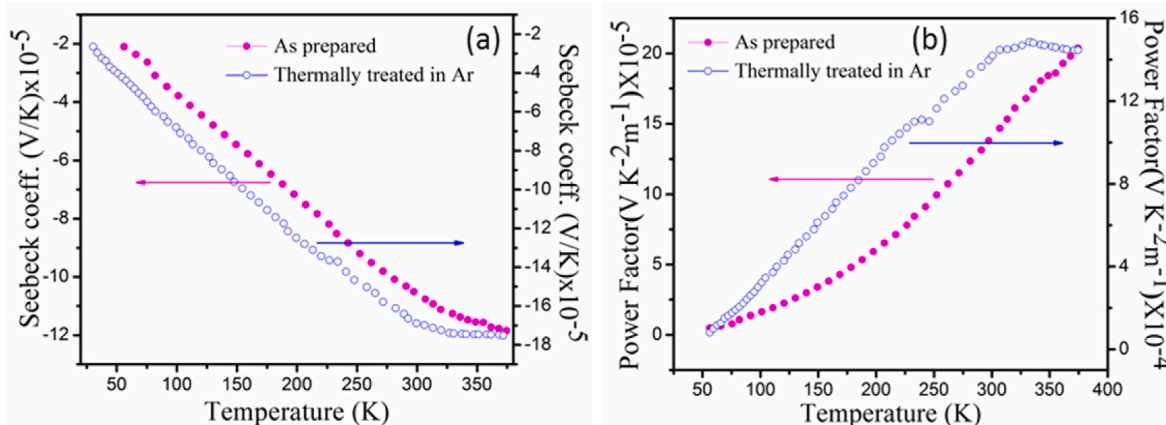


Fig. 9. Temperature dependence of (a) Seebeck coefficient and (b) Power factor for the 10 h milled Bi₂Te₃ nanostructures before and after thermal annealing.

showing the characteristics of a conductor. The lattice vibration increases with temperature, which resists phonon propagation in the solid and causes a reduction of lattice thermal conductivity (K_l). As stated earlier, the electronic thermal conductivity (K_e) of both the annealed and un-annealed samples increases with temperature. Due to the increase of both K_e and K_l , the total thermal conductivity (K) of the un-annealed sample increases with temperature.

On the other hand, with the increase of temperature, while the electronic contribution of thermal conductivity (K_e) increases for the annealed sample, its lattice thermal conductivity (K_l) decreases sharply, resulting in a net decrease of total thermal conductivity. For a given temperature, the total thermal conductivity of the annealed sample is considerably higher than the un-annealed sample. The higher value of K of the annealed Bi_2Te_3 nanostructures than the un-annealed one is mainly because of their higher K_l , which results from the grain growth due to thermal annealing and hence a reduction of phonon scattering at the grain boundaries. A similar effect has been reported earlier by Takashiri et al. [49] for their nanocrystalline bismuth-telluride thin films. At room temperature, the values of total thermal conductivity of 10 h milled un-annealed and annealed samples are ~ 0.67 W/K-m and ~ 2.30 W/K-m, respectively, which are pretty close to the reported values for nanostructured Bi_2Te_3 thin films [49].

3.3.3. Seebeck coefficient and power factor measurements

Fig. 9(a) presents the temperature dependence of Seebeck coefficients (α) for the 10h milled annealed and un-annealed samples. As can be seen, Seebeck coefficients of both the samples are negative, indicating electrons are majority charge carriers in both samples [50]. The Seebeck coefficient of both the samples increases almost linearly with the increase of temperature. Such an increase of Seebeck coefficient with temperature can be associated with the equation for the Seebeck coefficient of metals or highly degenerate semiconductors, expressed as:

$$\alpha = \frac{8\pi^2 K_B^2}{3eh^2} m^* T \left(\frac{\pi}{3n}\right)^{2/3} \quad (5)$$

where, m^* , T and n denote the effective mass of the carrier, absolute temperature, and carrier concentration, respectively [3], in parabolic band energy independent scattering approximation [51]. For a particular temperature, the absolute value of the Seebeck coefficient of the sample increases a bit after sintering, probably due to bigger crystallite/grain size, which causes a decrease of carrier concentration [49]. At room temperature, the absolute value of the Seebeck coefficient of the sample increases from 105.69 $\mu\text{V/K}$ to 168.78 $\mu\text{V/K}$ due to annealing, which is close to the previously reported values of Seebeck coefficient of nanocrystalline Bi_2Te_3 thin films [52,53].

From the obtained Seebeck coefficient (α) and electrical resistivity (ρ) values, power factor values (α^2/ρ) for the 10 h milled annealed, and un-annealed samples are calculated at different temperatures. The power factor is a significant thermoelectric parameter that determines the performance of a thermoelectric converter. The power factor values of the annealed and un-annealed samples at different temperatures are plotted in Fig. 9(b). For both samples, the power factor increases with temperature due to the positive values of $\Delta\alpha/\Delta T$ [54]. However, the power factor for the annealed sample is considerably higher in comparison to the same for the un-annealed sample for the whole range of measurement (30–375K). The higher power factor of the annealed sample can be associated with its higher Seebeck coefficient and lower electrical resistivity.

3.3.4. Thermoelectric figure of merit

Fig. 10 shows the temperature variation of the figure of merit (ZT) for 10 h milled Bi_2Te_3 sample before and after thermal treatment. The ZT value has increased with temperature for both samples. While the room temperature (300K) ZT value of the sample increased from 0.063 to 0.187 upon thermal annealing (at 573K in Ar), and the ZT value at 370K

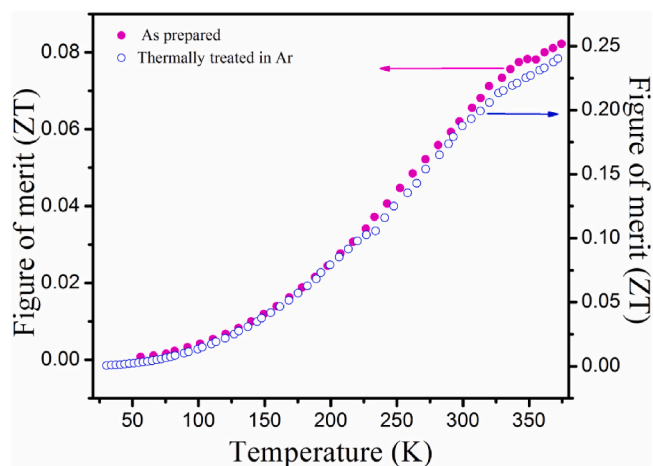


Fig. 10. Temperature variation of thermoelectric figure of merit (ZT) for the 10 h milled annealed and un-annealed Bi_2Te_3 samples.

Table 2

Estimated electrical and thermal transport parameters for the annealed and un-annealed Bi_2Te_3 nanostructures prepared by 10 h ball milling.

Physical properties	As prepared (unannealed) sample		Thermally annealed sample	
	At 300K	At 370K	At 300K	At 370K
Electrical resistivity ρ (in Ohm-m) (Error limit: ± 0.035)	7.974 x 10^{-5}	6.969 x 10^{-5}	1.946 x 10^{-5}	2.111 x 10^{-5}
Thermal Conductivity K (in W/K-m) (Error limit: ± 0.023)	0.6684	0.9115	2.299	2.235
Seebeck Coefficient α (in $\mu\text{V/K}$) (Error limit: ± 0.05)	-105.69	-118.00	-168.78	-174.56
Power Factor α^2/ρ (in $\text{V K}^{-2} \text{m}^{-1}$) (Error limit: ± 0.071)	14.042 x 10^{-5}	19.961 x 10^{-5}	14.194 x 10^{-4}	14.473 x 10^{-4}
Figure of Merit ZT (Error limit: ± 0.009)	0.063	0.082	0.187	0.239

increased from 0.08 to 0.239. The estimated ZT values of the annealed sample are similar to those reported earlier [55]. However, Zhou et al. [55] had reported comparatively higher ZT values for their mechanically alloyed (6 h milling and annealing in $\sim 327\text{K}$ – 427K temperature range) sample after rapid spark plasma sintering (SPS) at 663K. The higher ZT value of their Bi_2Te_3 samples might be associated with the rapid annealing process by the spark plasma treatment, where only a limited grain growth occurs. In the present case, the sample was pelletized with moderate unidirectional pressure and sintered at a comparatively lower temperature (573K) for 6 h. As the physical properties of a material depend on the synthesis method, different ZT values have been reported for Bi_2Te_3 prepared using different synthesis processes [19,21,27,56]. However, the ZT value (~ 0.239 at 370K) estimated for our annealed 10h ball-milled Bi_2Te_3 nanostructures is quite comparable to the reported ZT value (~ 0.25 at 370K) of Bi_2Te_3 synthesized by the solvothermal process [18]. It is also close enough with the reported value (~ 0.3 at 375K) of Bi_2Te_3 synthesized by mechanical alloying and SPS process [57]. The thermoelectric parameters estimated for the 10h milled Bi_2Te_3 nanostructures are presented in Table 2.

5. Conclusions

In summary, phase pure nanocrystalline Bi_2Te_3 could be successfully fabricated by solvent-free mechanical alloying of metallic Bi and Te

powder precursors under the Ar atmosphere. Formations of the Bi₂Te₃ phase and minor BiTe (I) and BiTe (II) phases have been noticed within the first 15 min of milling. Complete formation of single-phase Bi₂Te₃ nanostructures is observed only after 1 h of ball milling. A longer milling time produces smaller nanoparticles and introduces higher r.m.s. strain in the Bi₂Te₃ lattice. High-temperature thermal annealing under an inert atmosphere leads to extensive grain growth and helps to reduce the lattice strain of the Bi₂Te₃ nanostructures considerably, along with a reduction of phonon scattering in the lattice. Annealing also induces a metallic character to the ball-milled semiconducting Bi₂Te₃ nanostructures, resulting in reduced bandgap energy. The thermally annealed Bi₂Te₃ nanostructures manifest higher thermal conductivity than the as-prepared nanostructures, revealing the effect of grain growth on transport properties. Due to higher electrical conductivity and Seebeck coefficient, the thermally annealed Bi₂Te₃ nanostructures manifest better thermoelectric performance. The as-prepared and thermally annealed Bi₂Te₃ nanostructures manifest their n-type electrical conductivity and negative Seebeck coefficients. The power factor (α^2/ρ) of the annealed nanostructures is ~ 10 times higher (from $\sim 10^{-5}$ to $\sim 10^{-4}$) than that of the as-prepared sample. The thermoelectric figure of merit (ZT) of the annealed Bi₂Te₃ nanostructures is \sim three times higher than the un-annealed nanostructures in the 30–370K temperature range.

CRedit authorship contribution statement

Shrabani Paul: Investigation, Conceptualization, Methodology, Formal analysis, Writing – original draft. **Umapada Pal:** Conceptualization, Visualization, Writing – review & editing, Investigation, Resources. **Swapan Kumar Pradhan:** Conceptualization, Visualization, Writing – review & editing, Supervision, Validation.

Declaration of competing interest

The authors declare that they have no known competing financial interests or personal relationships that could have appeared to influence the work reported in this paper.

Acknowledgement

S. Paul and S. K. Pradhan wish to thank the Department of Science and Technology (DST) for the XRD facility under the FIST program. They also gratefully acknowledge the University Science Instrumentation Centre (USIC), The University of Burdwan, for providing FESEM with EDX facility generated through the DST sponsored PURSE program. U. Pal acknowledges the Consejo Nacional de Ciencia y Tecnologia (CONACyT), Mexico, for the financial helps extended through the project grants #CB-2017/2018-A1-S-26720 and # INFR-2014-02-23053. S. Paul extends her gratitude to the Higher Education Department, Government of West Bengal, for providing Swami Vivekananda Merit Cum Means Non-Net research fellowship to carry out the research work.

References

- J.-C. Zheng, Recent advances on thermoelectric materials, *Front. Phys. China* 3 (2008) 269–279.
- J.-F. Li, W.-S. Liu, L.-D. Zhao, M. Zhou, High-performance nanostructured thermoelectric materials, *NPG Asia Mater.* 2 (4) (2010) 152–158.
- G.J. Snyder, E.S. Toberer, Complex thermoelectric materials, *Nat. Mater.* 7 (2008) 105–114.
- J.Q. He, M.G. Kanatzidis, V.P. Dravid, High performance bulk thermoelectrics via a panoscopic approach, *Mater. Today* 16 (2013) 166–176.
- L.D. Zhao, V.P. Dravid, M.G. Kanatzidis, The panoscopic approach to high performance thermoelectrics, *Energy Environ. Sci.* 7 (2014) 251–268.
- I.T. Witting, T.C. Chasapis, F. Ricci, M. Peters, N.A. Heinz, G. Hautier, G.J. Snyder, The thermoelectric properties of bismuth telluride, *Adv. Electron. Mater.* 5 (2019) 1800904–1800923.
- R. Zybala, K. Mars, A. Mikula, J. Bogustawski, G. Soboń, J. Sotor, M. Schmidt, K. Kaszyca, M. Chmielewski, L. Ciupiński, K. Pietrzak, Synthesis and characterization of antimony telluride for thermoelectric and optoelectronic applications, *Arch. Metall. Mater.* 62 (2017) 1067–1070.
- Z.H. Dughaiash, Lead telluride as a thermoelectric material for thermoelectric power generation, *Physica B* 322 (2002) 205–223.
- D. Xia, C. Liu, S. Fan, A solar thermoelectric conversion material based on Bi₂Te₃ and carbon nanotube composites, *J. Phys. Chem. C* 118 (2014) 20826–20831.
- R. Amatyia, R.J. Ram, Solar thermoelectric generator for micropower applications, *J. Electron. Mater.* 39 (2010) 1735–1740.
- S.S. Sundaram, S.S. Kumar, A.S. Raj, K. Poovendhan, G. Udhayakumar, Solar energy powered mobile charging station using bismuth telluride-based thermoelectric generator, *Int. Res. J. Engg. Technol.* 6 (2019) 1085–1088.
- Y. Chen, X. Hou, C. Ma, Y. Dou, W. Wu, Review of development status of Bi₂Te₃-based semiconductor thermoelectric power generation, *Adv. Mater. Sci. Engg.* 2018 (2018) 1–9.
- A.N. Eddine, H. Sara, D. Chalet, X. Faure, L. Aixala, M. Cormerais, Modeling and simulation of a thermoelectric generator using bismuth telluride for waste heat recovery in automotive diesel engines, *J. Electron. Mater.* 48 (2019) 2036–2045.
- S.K. Bhukesh, A. Kumar, S.K. Gaware, Bismuth telluride (Bi₂Te₃) thermoelectric material as a transducer for solar energy application, *Mater. Today Proc.* 26 (2020) 3131–3137.
- L.D. Hicks, M.S. Dresselhaus, Effect of quantum-well structures on the thermoelectric figure of merit, *Phys. Rev. B* 47 (1993) 12727–12731.
- J.R. Sootsman, D.Y. Chung, M.G. Kanatzidis, New and old concepts in thermoelectric materials, *Angew. Chem.* 48 (2009) 8616–8639.
- Z.G. Chen, G. Han, L. Yang, L. Cheng, J. Zou, Nanostructured thermoelectric materials: current research and future challenge, *Prog. Nat. Sci.: Materials International* 22 (2012) 535–549.
- R. Jin, J. Liu, G. Li, Facile solvothermal synthesis, growth mechanism and thermoelectric property of flower-like Bi₂Te₃, *Cryst. Res. Technol.* 49 (2014) 460–466.
- H. Zou, D.M. Rowe, S.G.K. Williams, Peltier effect in a co-evaporated Sb₂Te₃(p)-Bi₂Te₃(n) thin film thermocouple, *Thin Solid Films* 408 (2002) 270–274.
- A. Foucaran, A. Sackda, A. Giani, F. Pascal-Delannoy, A. Boyer, Flash evaporated layers of (Bi₂Te₃-Bi₂Se₃)(N) and (Bi₂Te₃-Sb₂Te₃)(P), *Mater. Sci. Eng. B* 52 (1998) 154–161.
- L.M. Gonçalves, C. Couto, P. Alpuim, D.M. Rowe, J.H. Correia, Thermoelectric properties of Bi₂Te₃/Sb₂Te₃ thin films, *Mater. Sci. Forum* 514–516 (2006) 156–160.
- J.-J. Suñol, Mechanical alloying: processing and materials, *Metals* 11 (2021) 798–800.
- M.S. El-Eskandarany, A. Al-Hazza, L.A. Al-Hajji, N. Ali, A.A. Al-Duweesh, M. Banyan, F. Al-Ajmi, Mechanical milling: a superior nanotechnological tool for fabrication of nanocrystalline and nanocomposite materials, *Nanomaterials* 11 (2021) 2484–2518.
- J. Huot, F. Cuevas, S. Deledda, K. Edalati, Y. Filinchuk, T. Grosdidier, B. C. Hauback, M. Heere, T.R. Jensen, M. Lacroche, S. Sartori, Mechanochemistry of metal hydrides: recent advances, *Materials* 12 (2019) 2778–2821.
- A.R. Othman, A. Sardarinejad, A.K. Masrom, Effect of milling parameters on mechanical alloying of aluminum powders, *Int. J. Adv. Manuf. Technol.* 76 (2015) 1319–1332.
- S.S. Lin, C.N. Liao, Effect of ball milling and post treatment on crystal defects and transport properties of Bi₂(Se,Te)₃ compounds, *J. Appl. Phys.* 110 (2011) 93707–93713.
- B. Poudel, Q. Hao, Y. Ma, Y. Lan, A. Minnich, B. Yu, X. Yan, D. Wang, A. Muto, D. Vashaev, X. Chen, J. Liu, M.S. Dresselhaus, G. Chen, Z. Ren, High-thermoelectric performance of nanostructured bismuth antimony telluride bulk alloys, *Science* 320 (2008) 634–638.
- H. Li, H. Jing, Y.D. Han, Y. Xu, G.-Q. Lu, L. Xu, Microstructure and transport properties of copper-doped p-type BiSbTe alloy prepared by mechanical alloying and subsequent spark plasma sintering, *J. Alloys and Compd.* 576 (2013) 369–374.
- R. Venkatasubramanian, E. Siivola, T. Colpitts, B. O'Quinn, Thin-film thermoelectric devices with high room-temperature figures of merit, *nature* 413 (2001) 597–602.
- T.C. Harman, P.J. Taylor, M.P. Walsh, B.E. LaForge, Quantum dot superlattice thermoelectric materials and devices, *Science* 297 (2002) 2229–2232.
- K.F. Hsu, S. Loo, F. Guo, W. Chen, J.S. Dyck, C. Uher, T. Hogan, E. K. Polychroniadis, M.G. Kanatzidis, Cubic AgPb_mSbTe_{2+m}: bulk thermoelectric materials with high figure of merit, *Science* 303 (2004) 818–821.
- W. Kim, J. Zide, A. Gossard, D. Klenov, S. Stemmer, A. Shakouri, A. Majumdar, Thermal conductivity reduction and thermoelectric figure of merit increase by embedding nanoparticles in crystalline semiconductors, *Phys. Rev. Lett.* 96 (2006) 45901–45904.
- X. Tang, W. Xie, H. Li, W. Zhao, Q. Zhang, M. Niino, Preparation and thermoelectric transport properties of high-performance p-type Bi₂Te₃ with layered nanostructure, *Appl. Phys. Lett.* 90 (2007) 12102–12104.
- W. Xu, E. Nazaretski, M. Lu, Characterization of the thermal conductivity of La_{0.95}Sr_{0.05}CoO₃ thermoelectric oxide nanofibers, *Nano Res.* 7 (2014) 1224–1231.
- X.B. Zhao, X.H. Ji, Y.H. Zhang, T.J. Zhu, J.P. Tu, X.B. Zhang, Bismuth telluride nanotubes and the effect on the thermoelectric properties of nanotube-containing nanocomposites, *Appl. Phys. Lett.* 86 (2005) 62111–62113.
- S.K. Kanta, S. Paul, T. Chatterjee, H. Dutta, S.K. Pradhan, Microstructure and electrical characterization of thermoelectric nanocrystalline Bi₂Te₃ synthesized by mechanical alloying, *Mater. Res.* 22 (2019) 1–8.

- [37] L. Lutterotti, Total pattern fitting for the combined size–strain–stress–texture determination in thin film diffraction, *Nucl. Instrum. Methods Phys. Res. Sect. B Beam Interact. Mater. Atoms* 268 (2010) 334–340.
- [38] R.A. Youness, M.A. Taha, H. Elhaes, M. Ibrahim, Molecular modeling, FTIR spectral characterization and mechanical properties of carbonated-hydroxyapatite prepared by mechanochemical synthesis, *Mater. Chem. Phys.* 190 (2017) 209–218.
- [39] B.E. Warren, *X-Ray Diffraction*, Dover, INC., New York, 1990.
- [40] K. Sharma, A. Kumar, N. Goyal, M. Lal, Characterization and optical properties of Bi_2Te_3 and $(\text{Bi}_{1.20}\text{Sb}_{0.80})_2\text{Te}_3$, *AIP Adv.* 1536 (2013) 603–604.
- [41] K. Sharma, M. Lal, V.K. Gumber, A. Kumar, N. Chaudary, N. Goyal, Effect of composition on optical and thermoelectric properties of microstructured p-type $(\text{Bi}_2\text{Te}_3)_x(\text{Sb}_2\text{Te}_3)_{1-x}$ alloys, *J. Nano and Electronic Phys.* 6 (2014) 1007–1012.
- [42] F. Sansoz, Thermoelectrics and its energy harvesting; Materials, preparation and characterization in thermoelectronics, in: D.M. Row (Ed.), *Surface and Interface Effects on Thermoelectric Behavior in Crystalline Nanowires*, CRC Press, Taylor & Francis, Boca Raton, FL, 2012, pp. 15–22.
- [43] S.K. Mishra, S. Satpathy, O. Jepsen, Electronic structure and thermoelectric properties of bismuth telluride and bismuth selenide, *J. Phys. Condens. Matter* 9 (1997) 461–470.
- [44] M. Singh, M. Goyal, K. Devlal, Size and shape effects on the bandgap of semiconductor compound nanomaterials, *J. Taibah Univ. Sci* 12 (2018) 470–475.
- [45] D. Adler, H. Brooks, Theory of semiconductor-to-metal transitions, *Phys. Rev.* 155 (1967) 826–840.
- [46] J.H. Son, M.W. Oh, B.S. Kim, S.D. Park, B.K. Min, M.H. Kim, H.W. Lee, Effect of ball milling time on the thermoelectric properties of p-type $(\text{Bi,Sb})_2\text{Te}_3$, *J. Alloys Compd.* 566 (2013) 168–174.
- [47] J.H. Son, M.W. Oh, B.S. Kim, S.D. Park, Optimization of thermoelectric properties of n-type $\text{Bi}_2(\text{Te,Se})_3$ with optimizing ball milling time, *Rare Met.* 37 (2018) 351–359.
- [48] D.L. Medlin, G.J. Synder, Interfaces in bulk thermoelectric materials, A review for current opinion in colloid and interface Science, *Curr. Opin. Colloid Interface Sci.* 14 (2009) 226–235.
- [49] M. Takashiri, K. Miyazaki, S. Tanaka, J. Kurosaki, D. Nagai, H. Tsukamoto, Effect of grain size on thermoelectric properties of n-type nanocrystalline bismuth-telluride based thin films, *J. Appl. Phys.* 104 (2008) 84302–84307.
- [50] B.G. Kim, C.H. Lim, S.M. Choi, W.S. Seo, H.L. Lee, S.H. Hyun, S.M. Jeong, Free-standing Bi-Sb-Te films derived from a thermal annealing of sputter-deposited $\text{Sb}_2\text{Te}_3/\text{Bi}_2\text{Te}_3$ multilayer films for thermoelectric applications, *Cryst. Eng. Comm.* 17 (2015) 7522–7527.
- [51] M. Cutler, J.F. Leavy, R.L. Fitzpatrick, Electronic transport in semimetallic cerium sulfide, *Phys. Rev.* 133 (1964) A1143–A1152.
- [52] H.J. Goldsmid, Bismuth telluride and its alloys as materials for thermoelectric generation, *Materials* 7 (2014) 2577–2592.
- [53] H. Böttner, J. Nurnus, A. Gavrikov, G. Kühner, M. Jäggle, C. Künzel, D. Eberhard, G. Plescher, A. Schubert, K.H. Schlereth, New thermoelectric components using microsystem technologies, *J. Microelectromechanical Systems* 13 (2004) 414–420.
- [54] M. Scheele, A.M. Kreuziger, A. Kornowski, C. Klinke, H. Weller, ZT enhancement in solution-grown $\text{Sb}_{(2-x)}\text{Bi}_x\text{Te}_3$ nanoplatelets, *ACS Nano* 4 (2010) 4283–4291.
- [55] M. Zhou, J. Li, J. Liu, Thermoelectric properties of Bi_2Te_3 alloy prepared by mechanical alloying and spark plasma sintering, *Key Eng. Mater.* 368–372 (2008) 538–540.
- [56] M. Saleemi, M.S. Toprak, S. Li, M. Johnsson, M. Muhammed, Synthesis, processing and thermoelectric properties of bulk nanostructured bismuth telluride (Bi_2Te_3), *J. Mater. Chem.* 22 (2012) 725–730.
- [57] Z.-H. Ge, Y.-H. Ji, Y. Qiu, X. Chong, J. Feng, J. He, Enhanced thermoelectric properties of bismuth telluride bulk achieved by telluride-spilling during the spark plasma sintering process, *Scripta Mater.* 143 (2018) 90–93.